Supporting Information

Hudson et al. 10.1073/pnas.1715302115

SI Materials and Methods

Western Blot Analysis. Intestinal tissue for Western blotting was isolated from mice anesthetized with avertin and immediately transferred to ice-cold PBS with 1 mM PMSF. Whole intestines were dissected longitudinally and rinsed vigorously to remove luminal contents. The tissue was then cut into desired segmental lengths (usually 3 cm) transferred to 15-mL conical tubes containing 5 mL of dissociation buffer (1× PBS, 3 mM EDTA, 1 mM PMSF, and 1× Roche Complete EDTA-free protease inhibitor tablets) and mixed thoroughly. Tubes were mixed end-over-end in a 4 °C room for 45 min with vigorous shaking every 5 min. Mesenchyme was removed with forceps, and intestinal epithelial cells were collected by centrifugation at 1,000 × *g* at 4 °C for 5 min followed by snap freezing in LN_2 and storage at −80 °C. Cells were lysed by resuspending in 250 mM sucrose, 30 mM Histidine, pH 7.2, 1 mM PMSF, and 1× protease inhibitor tablet and passing through an 18G followed by a 22G syringe. Lysates were centrifuged at 6,000 × *g* for 5 min at 4 °C and supernatants collected and added to 5× SDS buffer followed by incubation at room temperature for 1 h (Dmt1 aggregates if heated to 95 °C). Primary antibodies detecting Dmt1 (a generous gift from P. Gros, McGill University, Montreal, Quebec, Canada), Bpnt1 (2296, J.D.Y. laboratory), and Actin (Sigma) were incubated overnight at 4 °C and analyzed by Li-COR.

RNA and qRT-PCR Analysis. Total duodenal RNA was extracted from tissues isolated as described above in Western blot analysis from a 1–2-mm strip of intestine immediately distal to the pyloric sphincter. RNA was extracted using TRIzol according to the manufacturer's recommendations (Life Technologies). Briefly, snap-frozen tissue segments were added to 20 volumes of TRIzol and rapidly homogenized using a PowerGen 700 homogenizer (Fisher Scientific, power "4") and disposable hard tissue generators (Omni International). cDNA was synthesized with the Bio-Rad iScript reverse trascriptase kit using random hexamers. Control (-)RTase reactions were included for each sample. Quantitative PCR was performed on a Bio-Rad iQ5 using the SsoFast Evagreen PCR supermix. Primers were generated using the NCBI Primerblast software and were designed to cross an intronic boundary. Primers were tested for linearity over 3 logs of dilution, and (-)RT reactions consistently yielded no amplified product.

Tissue and Serum Iron Quantification. Iron analysis was performed according to standard methodologies with minor modifications. Briefly, livers and spleens were isolated following PBS perfusion, blotted dry, and snap-frozen in liquid nitrogen. The tissues were weighed while still frozen and added to nine volumes of acid lysis buffer (3 M HCl, 0.61 M trichloroacetic acid). The samples were shaken vigorously and incubated at 95 °C overnight until completely dissociated. Samples were then centrifuged at 5,000 × *g* for 10 min. To quantify iron content, five volumes of saturated sodium acetate, five volumes of milliQ water, and one volume of chromogen stock solution (1.86 mM bathophenanthroline, 143 mM thioglycolic acid in milliQ water) were combined to generate the chromogen working solution. We then added 100 μL of supernatant to 1 mL of working chromogen buffer and incubated it for 10 min at room temperature to allow for color development. Absorbencies were measured on a Beckman Coulter DU730 spectrophotometer and compared with a standard curve of iron(II) sulfate ranging from 0 to 4,000 μg/dL Fe^{2+}. Samples above the linear range of the assay were diluted 1:10 with acid lysis buffer.

Hematological Parameters, Histology, and Immunohistochemistry. For hematological analysis, mice were killed by CO_2 exposure, and blood was collected by cardiac stick from the right ventricle. Blood was collected into K_2EDTA tubes (Becton Dickinson) and mixed gently to prevent clotting. CBCs were performed by the Duke Veterinary Diagnostic Laboratory using an Abbot Cell Dyn 3700. For blood smears, whole blood was collected via cardiac stick, spread onto glass slides (Fisher Scientific), allowed to air-dry, and stained with Wright-Giemsa (Electron Microscopy Services, Duke University). For histological analysis, mice were killed using the above method and then perfused transcardially with 30 mL of PBS, pH 7.4. Tissues for histology were fixed in 10% formalin (VWR) for 2 d and then embedded in paraffin by the Duke University Medical Center Immunohistology Research Laboratory. Sections of 5 μm were stained for Perls' iron by the Duke University Medical Center Immunohistology Research Laboratory. A section of iron-loaded human liver serves as a positive control for staining quality. For immunohistochemistry, sections were blocked, stained, and visualized with DAB according to standard procedures. Primary antibodies recognizing fibrillarin (Abcam), Bpnt1 (York laboratory-2296), or HIF-2α (Novus Biological) were incubated at 4 °C overnight. Slides were imaged on a Nikon TE2000 inverted microscope. Quantification was performed using Image-J (NIH).

Quantification of Iron Stores. Livers, spleens, and duodenums were isolated following PBS perfusion, blotted dry, and frozen in liquid nitrogen. The tissues were weighed while frozen and added to nine volumes of acid lysis buffer (3 M HCl, 0.61 M trichloroacetic acid). The samples were shaken vigorously and incubated at 95 °C overnight until completely dissociated. Samples were then centrifuged at 5,000 × *g* for 10 min. To quantify iron content, five volumes of saturated sodium acetate, five volumes of double-distilled water, and one volume of chromogen stock solution (1.86 mM bathophenanthroline, 143 mM thioglycolic acid in double-distilled water) were combined to generate the chromogen working solution. We then added 100 μL of supernatant to 1 mL of working chromogen buffer and incubated it for 10 min at room temperature to elicit a color change. Absorbance was measured on a Beckman Coulter DU730 spectrophotometer and compared with a standard curve of iron(II) sulfate ranging from 0 to 4,000 μg/dL Fe^{2+}. Samples above the linear range of the assay were diluted 1:10 with acid lysis buffer.

PAP Quantification. Tissue PAPS and PAP levels were measured using a combination of two previously published protocols (1, 2). Briefly, frozen intestine segments (~3 cm) were boiled for 3 min in 5 μL of PAP isolation buffer [50 mM glycine (pH 9.2)] per milligram of tissue and disrupted using a PowerGen 700 homogenizer (Fisher Scientific, power 4) and disposable hard tissue generators (Omni International). This process was repeated once more before transferring the samples to ice. Homogenates were clarified at 16,100 × *g*, 4 °C for 20 min. Following addition of 0.2 volumes of $CHCl_3$, mixtures were shaken vigorously and then centrifuged at 16,100 × *g*, 4 °C for 20 min. Finally, the upper aqueous phases were collected. The final extract was stable at −80 °C for at least 3 mo. PAP quantification was performed as described previously (3).

RNA-Seq and Analysis. PolyA-selected mRNA libraries were prepared with KAPA Biosystems sample kits using indexed adaptors (Illumina), pooled (12 libraries), and subjected to 75 bp paired-end sequencing according to the manufacturer's protocol (Illumina NextSeq500). Raw data and alignment quality control were performed using QC3 (4). Raw data were aligned with TopHat2 (5) against human transcript genome HG19, and read counts per gene were obtained using HTSeq (6). Differential expression analysis was performed using DESeq2 (7). We defined false discovery rate (FDR) as <0.05. Unsupervised cluster analysis was performed using Heatmap3 by selecting the top 5% of genes with the highest coefficient of variance (8). We performed gene ontology analysis using Database for Annotation, Visualization and Integrated Discovery (DAVID) as previously described (9, 10). GSEA was performed as previously described (11). GSEA enabled us to rank every transcript sequenced according to fold change and *P* value to determine the physiologically significant overlap in gene expression patterns of known biological pathways and functions.

The following Gene Ontology (GO) transcriptional signatures were used: (*i*) Iron metabolism: GO:0020037, heme binding; GO:0051536, iron–sulfur cluster binding, as well as genes involved in Bpnt1 biology (3, 12–14). (*ii*) The HIF-2α target genes were derived as previously described (15). (*iii*) Nucleolus, GO:0005730. (*iv*) Sulfate assimilation: transferase activity transferring sulfur containing groups, GO:0016782; sulfur metabolic process, GO:0006790; sulfur compound biosynthetic process, GO:0044272; oxidoreductase activity acting on a sulfur group of donors, GO:0016667; and KEGG sulfur metabolism. In addition, we compared our RNA-seq data with sequencing data from a HIF-2α intestine-specific knockout as previously described (16). In addition, we studied the Broad Institute Molecular Signatures Database C2 curated gene sets as well as manual input of genes known to be involved in Bpnt1 biology (3, 12, 13).

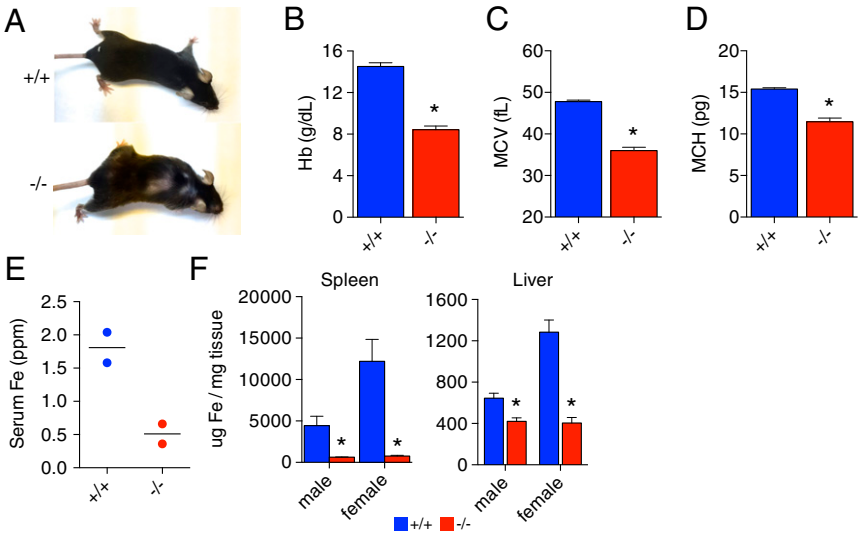

Fig. S1. One-year-old Bpnt1$^{-/-}$ mice have severe iron-deficiency anemia. (*A*) Representative photograph of Bpnt1$^{-/-}$ mice demonstrating profound alopecia. (*B–D*) Hematological parameters of wild-type and Bpnt1$^{-/-}$ animals. (*E*) Inductively coupled plasma mass spectrometry analysis of iron content in serum from Bpnt1$^{+/+}$ and Bpnt1$^{-/-}$ animals. (*F*) Tissue iron quantification from spleens and livers of male and female global knockouts. *$P < 0.05$.

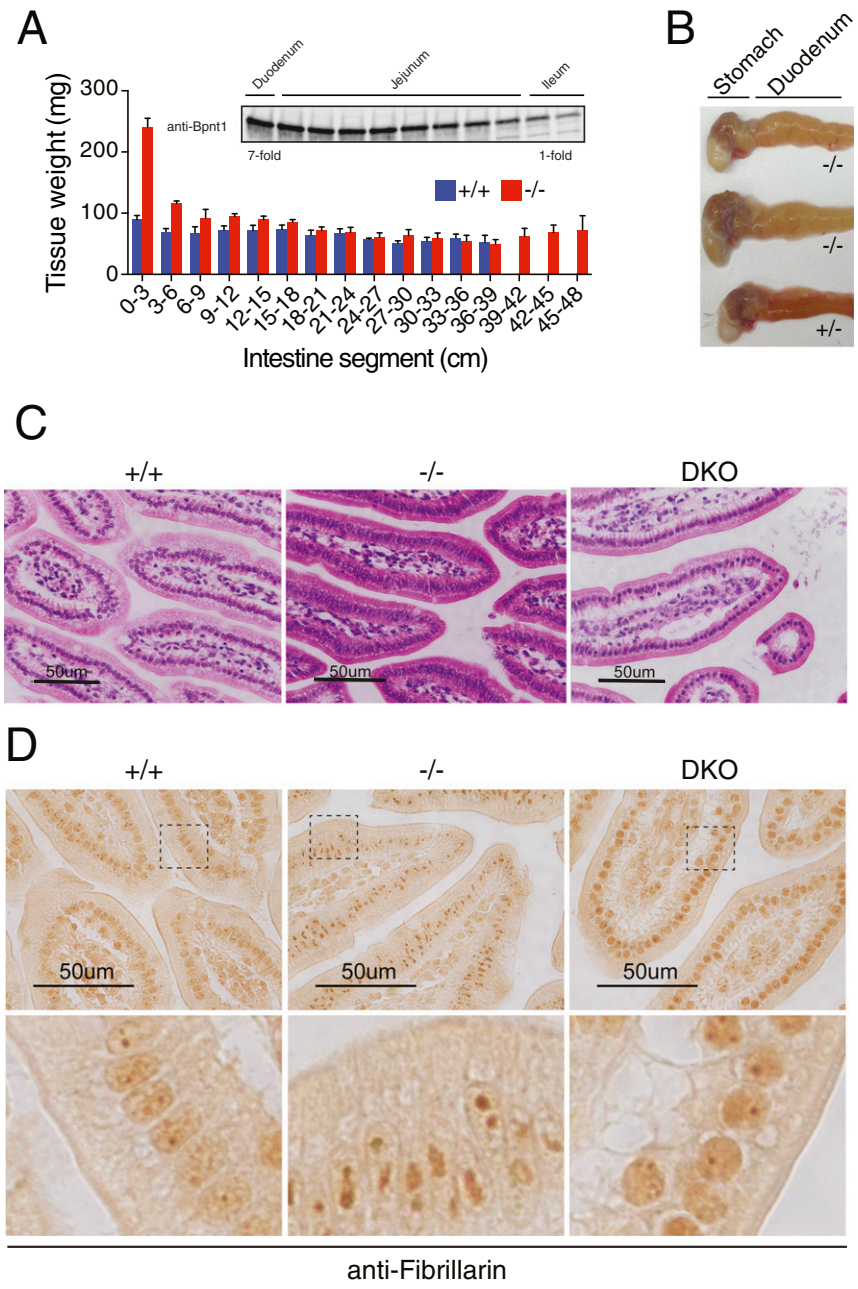

Fig. S2. Bpnt1 loss in mice results in abnormal intestinal architecture. (*A*) Dietary iron absorption occurs primarily in the duodenum, the proximal portion of the small intestine immediately distal to the stomach. Macroscopic comparison of wild-type and Bpnt1$^{-/-}$ intestinal architecture reveals that mutants are heavier, longer (~48 cm versus ~39 cm), and pale in color. This effect is most obvious in the proximal duodenum, which weighs on average ~twofold more than the matching segment of wild-type intestine. Average wet weights of 3-cm segments of wild-type ($n = 4$) or Bpnt1$^{-/-}$ mice ($n = 4$) demonstrating both heavier proximal sections and greater overall length in mutant animals. (*A*, *Inset*) Western blot for Bpnt1 demonstrating increased Bpnt1 protein expression in the proximal duodenum that decreases gradually distally through the small intestinal tract. (*B*) Photograph of Bpnt1 knockout (top two) and Bpnt1 heterozygous (bottom) gastroduodenal segments showing pale color and dilated appearance, demonstrating marked alteration of the intestinal architecture in Bpnt1$^{-/-}$ mice. (*C*) H&E staining of wild-type and Bpnt1$^{-/-}$ mice demonstrating profound changes in intestinal morphology in Bpnt1$^{-/-}$ mice that are rescued in the DKO mice. (*D*) Immunohistochemistry analysis of nucleoloar-resident fibrillarin in duodenal villi. Here, we report perturbed nucleolar architecture in Bpnt1-deficient gut enterocytes, an indicator of tissue-specific elevation of cellular PAP levels (14). (*D*, *Bottom*) Higher magnification of aberrant enterocyte nuclear and nucleolar architecture in global Bpnt1-deficient enterocytes that is rescued in the DKO animal. Scale of bottom panels is 23 × 21 μm (width × height) and indicates region denoted by dashed box in upper panels.

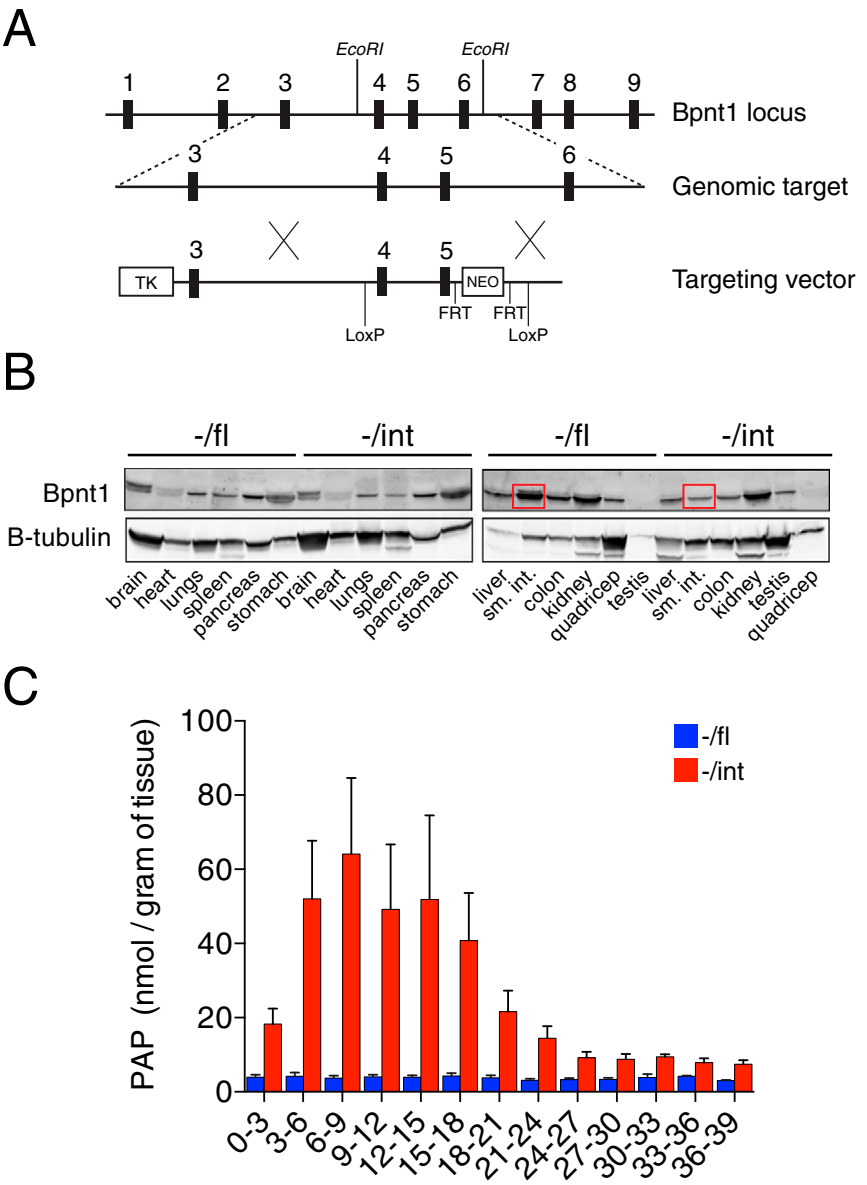

Fig. S3. Generation and confirmation of intestine-specific Bpnt1 knockout mice. (*A*) Genomic targeting strategy to introduce LoxP sites flanking the fourth and fifth exons of the Bpnt1 locus. NEO, neomycin resistance cassette for positive selection; TK, thymidine kinase cassette for negative selection. Floxed mice were then crossed with mice expressing Cre recombinase under the control of the villin promoter to generate intestine-specific knockouts. (*B*) Representative Western blot analysis of tissues from Bpnt1$^{-/fl}$ and Bpnt1$^{-/int}$ mice demonstrating a significant decrease in expression of Bpnt1 in whole small intestine. Appearance of incomplete knockout is due to residual Bpnt1 protein in intestinal cell types that do not express villin. (*C*) PAP analysis in the small intestines of Bpnt1$^{-/fl}$ and Bpnt1$^{-/int}$ mice demonstrating robust elevation of PAP in the proximal small intestine (n = 3).

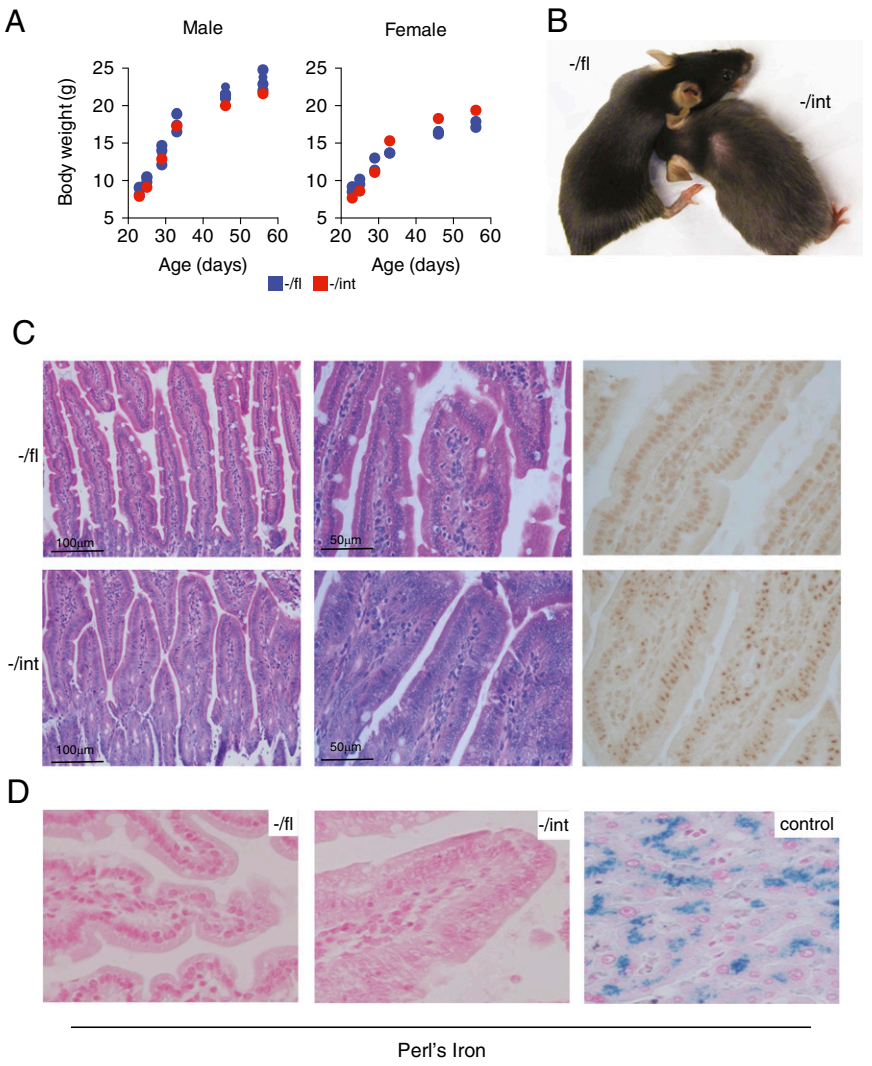

Fig. S4. Bpnt1$^{-/int}$ mice display altered intestinal morphology. (*A*) Analysis of body weight after weaning in male and female intestine-specific knockout mice. Bpnt1$^{-/int}$ mice have no obvious growth defects or abnormalities through 8 wk postnatal. (*B*) Representative photograph of 8-wk-old mice demonstrating alopecia in Bpnt1$^{-/int}$ mice. (*C*, *Left*) H&E staining of wild-type and Bpnt1$^{-/int}$ proximal duodenum demonstrating profound changes in cellular architecture and brush border changes. (*C*, *Right*) Fibrillarin staining of wild-type and Bpnt1$^{-/int}$ mice demonstrating aberrant nucleolar condensation in Bpnt1$^{-/int}$ mice. Scale of *C*, *Right* is the same as *C*, *Middle*. (*D*) Photograph of Perls' iron stained duodenal villi. Note the lack of detectable iron staining in Bpnt1$^{-/int}$ mice. The positive control section is iron-loaded, human liver. Donovan et al. (15) reported that a defect in the basolateral iron transporter, Fpn, leads to sequestration and accumulation of iron in the enterocyte (17). Our RNA-seq data showed that loss of Bpnt1 resulted in defects in apical iron transporter, Dmt1, as well as decreased Fpn expression. Thus, we expected no accumulation of iron in the Bpnt1$^{-/int}$ mouse because iron was unable to be absorbed into the enterocyte. Magnification and scale are the same as in *C*, *Middle*.

A

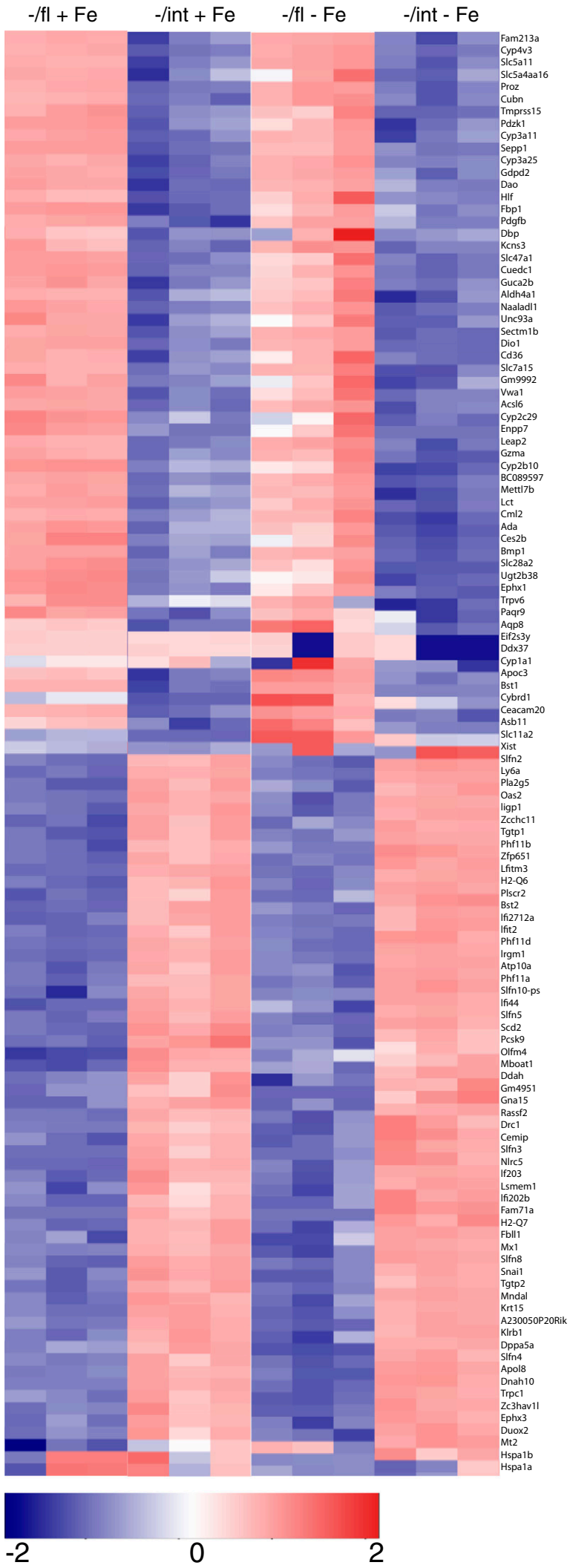

B

Category	Term	# Genes	p-value
GOTERM_MF_FAT	Porphyrin binding	8	9.50E-06
GOTERM_MF_FAT	Aromatase activity	5	2.30E-05
GOTERM_MF_FAT	Iron Ion Binding	10	4.60E-05
GOTERM_MF_FAT	Heme Binding	7	7.80E-05
GOTERM_BP_FAT	Oxidation Reduction	13	7.00E-05
GOTERM_BP_FAT	Response to Iron ion	2	1.40E-02
GOTERM_CC_FAT	Brush Border	5	1.80E-05
KEGG_PATHWAY	Metabolism of xenobiotics by cytochome P450	6	7.70E-06
KEGG_PATHWAY	Retinol Metabolism	5	1.90E-04
KEGG_PATHWAY	Linoleic Acid Metabolism	4	9.80E-04
KEGG_PATHWAY	Drug Metabolism	4	4.00E-03
KEGG_PATHWAY	PPAR signaling pathway	4	4.60E-03

C

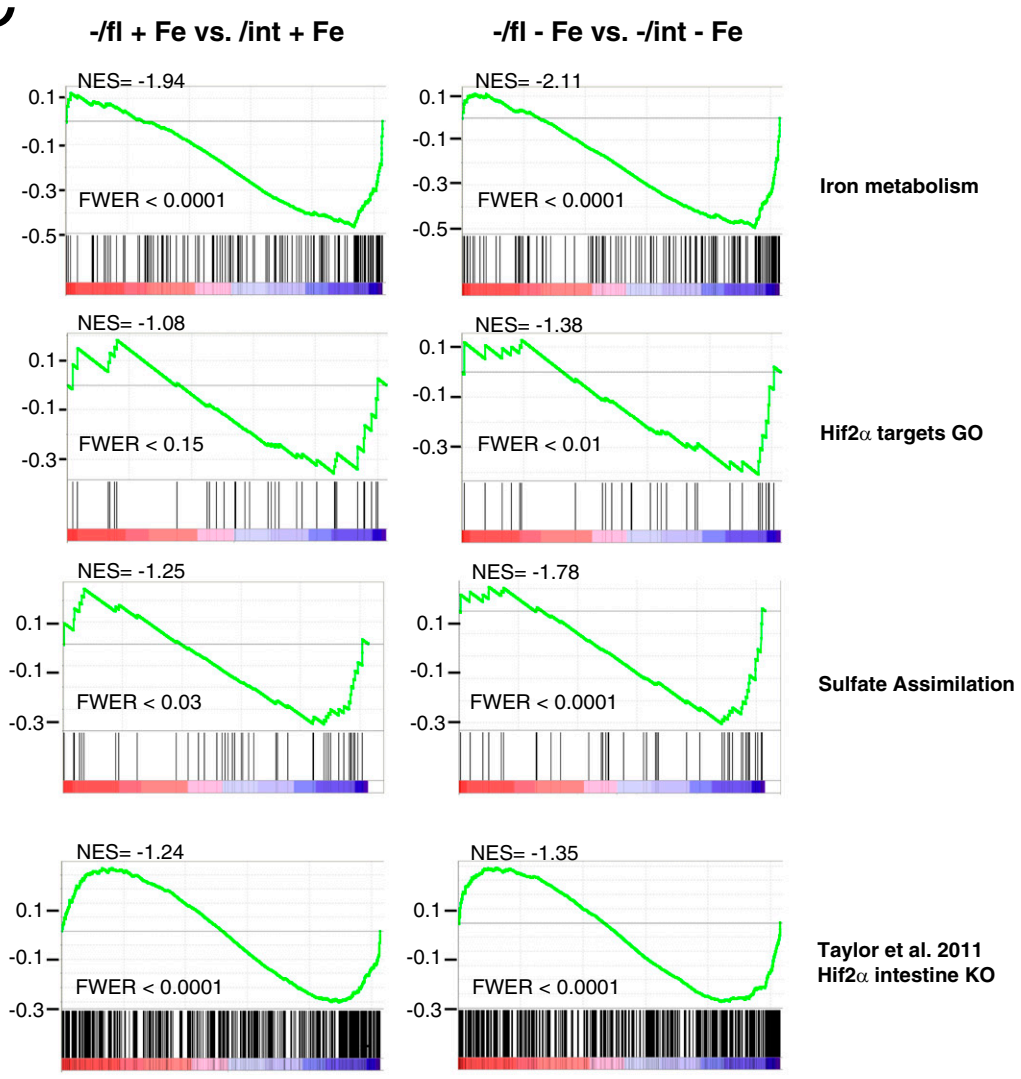

D

Category	Term	# Genes	p-value
UP_SEQ_FEATURE	Glycosylation site	29	8.0E-03
UP_SEQ_FEATURE	Signal peptide	24	2.9E-02
UP_SEQ_FEATURE	Disulfide bond	19	6.6E-02
UP_SEQ_FEATURE	Heme axial ligand	3	9.5E-02
GOTERM_MF_FAT	Iron ion binding	7	8.1E-03
GOTERM_MF_FAT	Iron ion transmembrane transporter activity	2	3.5E-02
GOTERM_BP_FAT	Response to iron ion	2	1.6E-02
GOTERM_BP_FAT	Iron ion transport	3	1.3E-02
SP_PIR_KEYWORDS	Iron transport	3	4.4E-03
SP_PIR_KEYWORDS	Iron	7	5.4E-03

Fig. S5. Bpnt1$^{-/int}$ enterocytes display broad changes in transcriptional activity. (*A*) Heatmap displaying top 5% of genes that changed between enterocytes of Bpnt1$^{-/fl}$ vs. Bpnt1$^{-/int}$ mice fed either an iron-replete or iron-deficient diet for 5 wk ($n = 3$ per group). (*B*) DAVID gene ontology analysis on the genes in *A* highlighting changes in biological processes related to iron metabolism between Bpnt1$^{-/fl}$ and Bpnt1$^{-/int}$ mice fed either an iron-replete or iron-deficient diet for 5 wk. (*C*) GSEA was used to compare the transcriptional signature of Bpnt1$^{-/int}$ enterocytes to gene ontology signatures of iron metabolism, HIF-2α, sulfate assimilation, and sequencing data from HIF-2α$^{-/int}$ animals published by ref. 17. Enrichment score is plotted on the *y* axis, and each vertical line along the *x* axis represents an individual gene. (*D*) DAVID analysis of the shared subset of genes (92) described in Fig. 4*C*. DAVID gene ontology analysis confirmed that the shared subset of genes in HIF-2α$^{-/int}$ and Bpnt$^{-/int}$ animals is intricately involved in iron metabolism.

		Normal chow			Fe-deficient chow		
		Fold Change	log2 Fold Change	p value	Fold Change	log2 Fold Change	p value
Canonical HIF-2α targets	Alas2	1.324453827	0.40539755	0.66616449	0.916666668	-0.12553088	0.60118538
	Epas1	0.339088925	-1.56026443	0.00000000	0.234659137	-2.09136146	0.00000000
	Epo	0.425778719	-1.23182425	0.00458135	0.331341235	-1.59361034	0.00876784
	Epor	1.834727697	0.87556596	0.29531787	1.923738484	0.94391269	0.65842612
	Fech	0.616836837	-0.69703917	0.00000019	0.722448979	-0.46903239	0.00000000
	Hba-a1	0.426269953	-1.23016073	0.01619693	0.207920792	-2.26589406	0.00259314
	Hba-a2	0.177238918	-2.49623267	0.00862805	0.139534884	-2.84130225	0.00097100
	Slc25a37	2.304376372	1.20437637	0.00000000	4.387931032	2.13354085	0.00000000
	Slc25a38	0.995641286	-0.00630204	0.97004617	1.16372093	0.21874513	0.09624013
HIF family members	Hif1a	1.507448307	0.59210853	0.00089307	1.312894099	0.39275055	0.46749888
	Hif1an	0.826227114	-0.27538969	0.03950493	0.720817729	-0.47229360	0.00037678
	Hif3a	2.357207628	1.23707884	0.04147384	1.409666989	0.49535439	0.36573067
HIF-2α Gene Ontology targets	Apex1	5.124278901	2.35734900	0.00000000	2.967317146	1.56915913	0.00000000
	Arnt	0.80128187	-0.31961826	0.02209683	0.802797756	-0.31689151	0.04067043
	Abcg2	0.340669549	-1.55355510	0.00000000	0.340032557	-1.55625521	0.00000000
	Bhlhe40	0.557707783	-0.84241869	0.00041404	0.887722445	-0.17181942	0.23876492
	Cited2	0.541050289	-0.88616540	0.00001220	0.470758546	-1.08694081	0.00000000
	Crebbp	0.993532475	-0.00936097	0.94905788	1.024581914	0.03503533	0.81367677
	Cul2	1.530085127	0.61361192	0.00001720	1.211735669	0.27707502	0.07854539
	Eif3e	2.305999787	1.20539238	0.00000000	1.831931336	0.87336543	0.00000094
	Efna1	0.40003003	-1.32181979	0.00000000	0.299727587	-1.73827622	0.00133394
	Egln1	0.782078013	-0.35461557	0.01508751	0.551835812	-0.85768901	0.00000004
	Egln2	0.642650768	-0.63789314	0.00017454	0.725351043	-0.46324872	0.00016309
	Egln3	0.265367028	-1.91393897	0.00000000	0.330731178	-1.59626904	0.00413345
	Elk1	2.249496574	1.16960217	0.00009870	1.787045181	0.83757611	0.00555204
	Ep300	1.062673341	0.08769819	0.63782639	0.968912688	-0.04556143	0.85398371
	Ets1	0.212050803	-2.23751815	0.00000000	0.222723597	-2.16667368	0.00000050
	Flt1	1.148397759	0.19962242	0.82013774	0.710992231	-0.49209430	0.56947177
	Fxn	2.122804129	1.08597126	0.00000035	2.217511306	1.14894146	0.00000181
	Kdr	0.716878078	-0.48020032	0.47252928	1.285120081	0.36190317	0.56018222
	Mmp14	0.995794126	-0.00608059	0.97116155	1.145144781	0.19553001	0.16272921
	Pgk1	0.930595141	-0.10377444	0.45637573	0.833753576	-0.26230705	0.03782296
	Pou5f1	1.108710203	0.14888232	0.86371144	1.086546155	0.11974946	0.88773231
	Rbx1	1.707735378	0.77208444	0.00000006	1.606541537	0.683958282	0.88773231
	Rps27a	2.79820242	1.48450033	0.00000000	2.427872449	1.27969263	0.00000000
	Sirt1	0.843002725	-0.24639080	0.14553125	0.830613163	-0.26775136	0.13477989
	Slc11a2	0.399849215	-1.32247204	0.00000000	0.165060548	-2.59893276	0.00029955
	Slc2a1	2.056142495	1.03994025	0.00000000	1.99518978	0.99652598	0.00000000
	Sp1	1.165427331	0.22085905	0.17983662	0.974635934	-0.03706468	0.81272555
	Serpine1	0.551322884	-0.85903061	0.05256612	1.123490519	0.16798795	0.82254253
	Tceb1	1.319287773	0.39975929	0.00829574	1.119385636	0.16270714	0.34537547
	Tceb2	0.987850385	-0.01763554	0.92551412	1.087232524	0.12066052	0.41642491
	Uba52	1.370972554	0.45519969	0.00935380	1.459089985	0.54506886	0.00205065
	Ube2d1	1.258686817	0.33191936	0.05908987	1.241381318	0.31194634	0.06615203
	Ube2d2a	1.067525647	0.09427073	0.45827651	0.970015624	-0.04392011	0.71452840
	Ube2d3	0.98328059	-0.02432493	0.85058723	0.952966781	-0.06950217	0.57651479
	Vegfa	0.18065622	-2.46868117	0.00000000	0.262566628	-1.92924453	0.00000000
	Vhl	0.945537276	-0.08079376	0.62233202	0.853387888	-0.22872646	0.17489223

Fig. S6. Accumulation of PAP in Bpnt1$^{-/int}$ enterocytes demonstrates broad changes in HIF-2α-associated gene targets. Summarized RNA-seq data (Fig. S5) for canonical HIF-2α target genes, other members of the HIF family, additional HIF-2α ontology terms, and manually curated genes associated with hypoxia signaling. Data are expressed as fold change and $\log_2$ fold change as analyzed by DESeq (n = 3 per group).